Novel Size and Surface Oxide Effects in Silicon Nanowires as Lithium Battery Anodes

Matthew T. McDowell,[†,§] Seok Woo Lee,[†,§] Ill Ryu,[†] Hui Wu,[†] William D. Nix,[†] Jang Wook Choi,*,[‡] and Yi Cui*,[†]

[†]Department of Materials Science and Engineering, Stanford University, Stanford, California 94305, United States

[‡]Graduate School of Energy, Environment, Water and Sustainability, Korea Advanced Institute of Science and Technology, 373-1 Guseong Dong, Yuseong Gu, Daejeon 305-701, Republic of Korea

S *Supporting Information*

ABSTRACT: With its high specific capacity, silicon is a promising anode material for high-energy lithium-ion batteries, but volume expansion and fracture during lithium reaction have prevented implementation. Si nanostructures have shown resistance to fracture during cycling, but the critical effects of nanostructure size and native surface oxide on volume expansion and cycling performance are not understood. Here, we use an ex situ transmission electron microscopy technique to observe the same Si nanowires before and after lithiation and have discovered the impacts of size and surface oxide on volume expansion. For nanowires with native SiO_2, the surface oxide can suppress the volume expansion during lithiation for nanowires with diameters $<\sim 50$ nm. Finite element modeling shows that the oxide layer can induce compressive hydrostatic stress that could act to limit the extent of lithiation. The understanding developed herein of how volume expansion and extent of lithiation can depend on nanomaterial structure is important for the improvement of Si-based anodes.

KEYWORDS: Energy storage, Li-ion batteries, nanowires
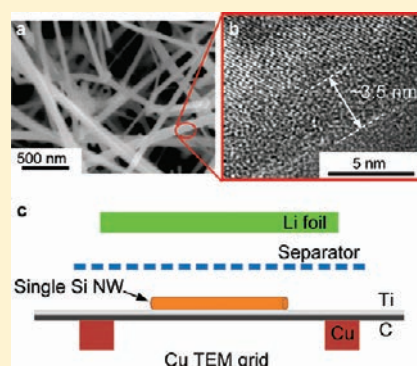
Rechargeable Li-ion batteries are currently one of the most important energy storage devices for portable electronics. However, to power more demanding applications, such as electric vehicles, Li-ion batteries with higher specific energy or energy density are required.[1,2] This can be achieved by utilizing electrode materials that have a higher specific capacity than current commercial electrode materials.[3−5] Alloying negative electrode materials, which react with lithium at low potentials and typically have much higher specific capacities than graphite, have the capability to significantly improve the specific energy of Li-ion batteries.[6−10] Si is a promising alloying anode material due to its high theoretical specific capacity of 4200 mAh g^{-1} (about ten times that of graphite), but like many alloying anodes, a large volume expansion during the Li reaction process can lead to fracture of large Si particles or films and loss of capacity with cycling.[6] Recently, various nanostructured Si anodes have been shown to exhibit good performance due to their resistance to fracture and pulverization during volume expansion.[7,8,11−15] Among them, Si nanowires (NWs) and nanotubes (NTs) are especially interesting; they can accommodate volume expansion better than larger Si structures, and their one-dimensional character facilitates axial charge transport and short radial Li ion diffusion distances.[8,13,16]

Although it is widely recognized that the volume change during alloying/dealloying is the major challenge limiting the implementation of Si-based anodes,[6,17,18] the nature of volume changes in nanostructured Si anodes is not well understood. This is important because the size and shape of nanostructured

particles can affect the stresses, strains, and volume expansion during lithiation; this in turn is closely linked to the pulverization behavior and cycle life of the electrode.[13,19−23] Modeling of the stresses in NWs during lithiation has shown that for small nanostructures, surface tension can induce compressive stress, which inhibits crack propagation and could extend cycle life.[21] In addition, there have been a few experimental studies examining volume changes in Si anodes of different morphologies. One study found that Si NTs can experience anisotropic expansion in the axial and radial directions.[13] Other research utilizing in situ atomic force microscopy to monitor amorphous Si thin films during lithiation and delithiation showed that the volume of the film expanded and contracted reversibly, in contrast to a Sn film.[24] Recently, it was shown that crystalline Si nanopillars and other structures have a tendency to expand along ⟨110⟩ crystallographic directions when lithiated.[25−27] In addition, in situ transmission electron microscopy (TEM) experiments have revealed the effects of doping and conductive coating on the lithiation behavior.[28] These studies have shown the importance of experimentally probing the expansion behavior of individual nanostructures, which is necessary for precise volume change measurements and for determining nanoscale size effects on expansion and contraction. Also, since the Si surface has a 2−5 nm thick native SiO_2 layer,[29] it is important to design
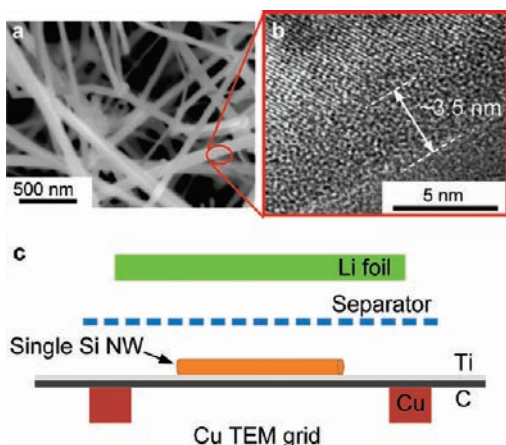
Figure 1. Single-NW-based ex situ TEM technique to study the effects of NW diameter and surface oxide on dimensional expansion during reaction with Li. (a) An SEM image of VLS-grown Si NWs shows that the growth process intrinsically produces Si NWs with various diameters. (b) A high-resolution TEM image of the surface of a Si NW showing a ~3.5 nm thick native oxide layer that accompanies the growth process. (c) A schematic illustration of a half cell for lithiating/delithiating single Si NWs on TEM grids. Using this technique, the same NW can be characterized before and after lithiation or delithiation.

experiments to determine the effect of an oxide layer on volume expansion and electrochemical characteristics. There have been studies showing that an SiO_2/carbon dual-layer coating can result in a mechanically stable SEI layer on Si nanoparticles,[30,31] but the effect of the oxide on Si volume change has thus far been neglected. In this paper, we utilize TEM to monitor volume changes in the same Si NWs before and after reaction with Li to determine the effects of NW size and surface oxide on the volume expansion characteristics, and we relate these data to the electrochemical behavior and cycle life to indicate promising routes for electrode improvement.

Si NWs are grown using the vapor—liquid—solid (VLS) method; in this process, a metal catalyst is saturated with Si atoms in the liquid phase, and a solid NW nucleates and grows from the catalyst particle.[32] A scanning electron microscopy (SEM) image of VLS-grown Si NWs is shown in Figure 1a. Si NWs that are exposed to air are covered with a thin (2—5 nm) amorphous oxide, as shown in the TEM image in Figure 1b.[29] In many studies, as-grown NWs with a range of diameters and native oxide-covered surface have been used as Li-battery anodes.[8,33,34] Although this approach has yielded good results, some key factors that could affect volume expansion characteristics and cycle life have not been explored.

To understand how size and surface characteristics affect volume changes in Si NWs, we have developed a method to follow the dimensional changes of single Si NWs by TEM examination of the same NW before and after electrochemical reaction; this technique provides direct and clear structural correlation and is distinct from most studies based on tests of ensemble Si electrodes.[7,8,12,13] First, Cu TEM grids with 15 to 25 nm carbon support films were covered with a thin (~20 nm) Ti layer that minimizes contact resistance between the Si NWs and the substrate; this layer is inert to lithium reaction while allowing TEM electron beam transmission. Si NWs were dispersed on the grids and imaged in a TEM, and their size and structure were recorded. The grids with NWs on them were inserted into

electrochemical half cells with Li metal foil as the counter electrode, as shown in the schematic in Figure 1c. The voltage of the Si NW electrode was then swept to 10 mV versus Li/Li^+ from the open circuit voltage at 0.2 mV/s and was held at 10 mV for 48 h to ensure reaction of the NWs with Li. The grids were then removed and washed with acetonitrile, and the same NWs were located and imaged again in a TEM. Because of the negligible mass of the few Si NWs at the working electrode, the resulting current signal during the lithiation process was too small to be detected, so TEM selected-area electron diffraction (SAED) was used to confirm that this potentiostatic treatment causes each NW to react with Li since Si undergoes a crystalline-to-amorphous phase transformation upon lithium insertion (this is shown by the SAED pattern and TEM images in Supporting Information Figure S1).[8,33,35−39] In this way, TEM characterization is sufficient to show that each NW is lithiated to the extent that it becomes amorphous; however, the actual extent of lithiation beyond amorphization is determined by the fixed holding potential and the local electrochemical potential of Li in each NW. This technique is unique because it allows us to track morphological changes in the same NW upon Li reaction and cycling and is therefore a powerful method to study volume changes in these NWs.

To clearly understand the dimensional changes after lithiation of NWs with different surfaces, we performed ex situ TEM measurements on NWs without surface oxide, with native oxide, and with thermally grown oxide. The oxide-free NWs were treated with HF before cycling to remove the native oxide, leaving the surface H-terminated.[29] Supporting Information Figure S2 shows a TEM image of an etched NW with oxide-free surfaces. For these experiments, the NWs were lithiated (charged) by the linear-sweep voltammetry method described previously and then imaged in the lithiated state. Figure 2a,b shows TEM images before and after lithiation of NWs with native oxide (Figure 2a) and without any oxide (Figure 2b), and Supporting Information Figure S1 contains additional images of similar NWs before and after lithiation. As previously mentioned, the NWs become amorphous after the lithiation procedure, confirming that the oxide layer does not block the transport of electrons into the NWs during lithiation. The diameter change was measured for NWs of varying size; Figure 2c is a plot of the final-to-initial diameter ratio versus initial diameter. It is clear from Figure 2c that the NWs with native oxide show size-dependent diameter expansion behavior, while the NWs with bare surfaces do not. For NWs with native oxide, smaller NWs expand to a lesser degree than larger NWs, while oxide-free NWs of all sizes expand to about the same diameter ratio (~1.7). To verify the oxide effect on the diameter expansion behavior, more experiments were carried out in which the native oxide was first removed from the surface of Si NWs, and then oxides of different thicknesses were grown on the surface by annealing the NWs in air at various temperatures (Supporting Information Figure S2 shows TEM images of NWs with ~3.4, ~4.5, and ~7.5 nm thick oxide grown this way). Figure 2d shows the final-to-initial diameter ratio for NWs with 0, ~3.4, and ~7.5 nm oxide; these results are similar to NWs with native oxide, but the NWs with thicker oxide expand to a lesser degree across most of the diameter range. It should be noted that anisotropic radial expansion along ⟨110⟩ directions could be occurring in these NWs, as has been reported in recent studies.[25,27] While this could slightly affect the measured radial expansion values, the expansion trends in NWs with and without oxide are not expected to be significantly affected.
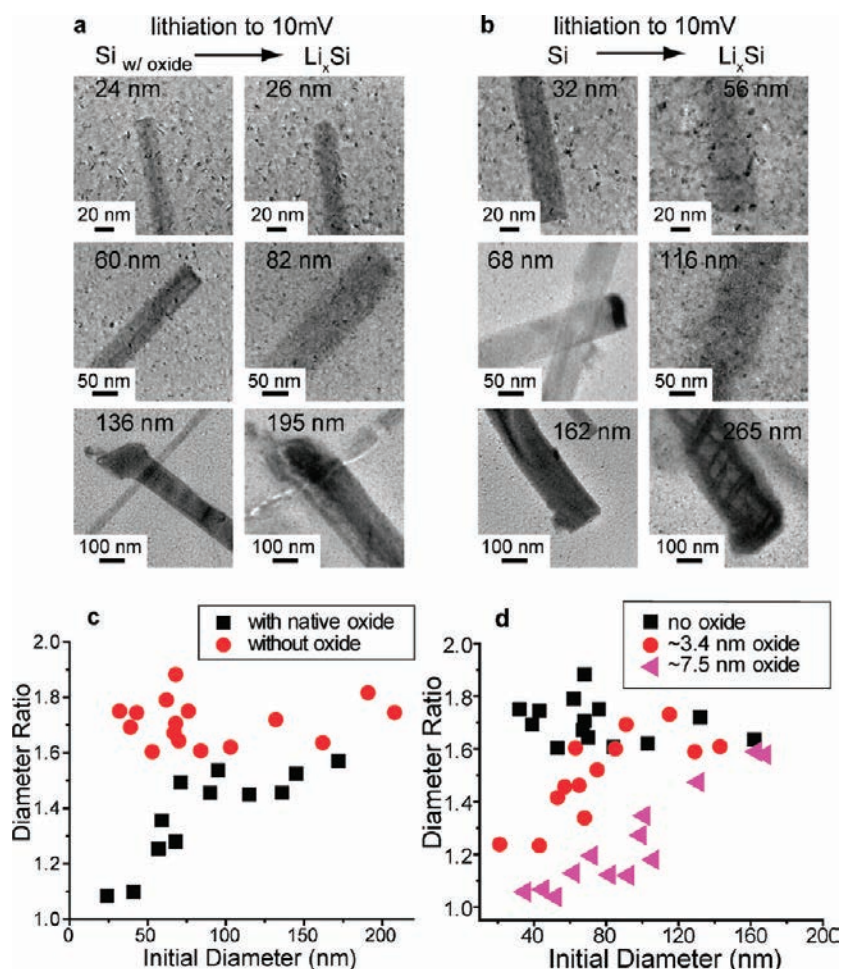
Figure 2. The effect of an oxide layer on the diameter expansion of Si NWs after lithiating at 10 mV vs Li/Li$^+$. (a,b) TEM images of Si NWs of various diameters before and after lithiating at 10 mV vs Li/Li$^+$. The NWs in (a) have ~3.5 nm native oxide, while the NWs in (b) were etched with HF to remove the native oxide. The values in the images denote the measured diameter of the NWs. (c) Plot showing the diameter change of Si NWs of various initial diameters after lithiating at 10 mV in the presence and absence of native oxide. The diameter changes are shown as a ratio of final to initial diameter. (d) Diameter changes after lithiating at 10 mV for Si NWs with different thermally grown oxide thicknesses.

In addition to diameter changes, length changes were also measured. Figure 3a shows that the final-to-initial length ratio for both native oxide and oxide-free NWs follows the same trend: the NWs show length contraction upon lithiation with larger NWs contracting to a greater degree. The final-to-initial volume ratio was calculated based on the diameter and length change for both types of NWs, and these data are presented in Figure 3b. Again, it is evident from this plot that NWs with native oxide exhibit diameter-dependent volume expansion in which smaller NWs expand to a lesser degree than larger NWs, while oxide-free NWs expand to an approximately constant volume ratio for all sizes. To summarize these data, schematics illustrating the dimensional changes in NWs with different diameters and surface character are shown in Figure 3c,d. Overall, the expansion data show that both diameter and surface oxide play an important role in the resulting dimensional changes upon lithiation; this fundamental behavior has not previously been observed in Si electrodes.

The observed length contraction in larger NWs upon lithiation (Figure 3a) is surprising because both radial and axial expansion would be expected. Other work has revealed that Si NTs show anisotropic volume change behavior on the first lithiation;[13] however, expansion still occurred in all directions.

In our recent work, we have used ex situ SEM techniques to study lithiation-induced volume changes in well-defined single-crystalline Si nanopillars with widths of ~400 nm. In this case, slight length contraction after lithiation was also observed.[25] We postulate that the single-crystalline nature of the NWs could play a role in this axial contraction. However, more research to understand and explain this phenomenon is currently underway.

To understand the effect of the oxide on diameter expansion, it is important to recognize how Li interacts with silicon oxide. Neutron diffraction and X-ray photoelectron studies have shown that a variety of compounds are formed when amorphous SiO is lithiated.[40−42] Li reacts with Si that is in an oxygen-deficient local environment to form Li−Si compounds, but Li is also consumed to form Li_2O and lithium silicates; these compounds are relatively inert and do not give up a significant amount of Li upon delithiation.[40,41] Also, the initial lithiation of SiO induces only about half the volume expansion of Si lithiation.[41] Another study on the lithium electrochemistry of SiO_2 thin films showed that $Li_2Si_2O_5$ was formed upon lithiation.[43] The surface oxide on the NWs in our study probably behaves in a similar manner; Li reacts to form silicates and Li_2O amid a framework of Li−Si. In any
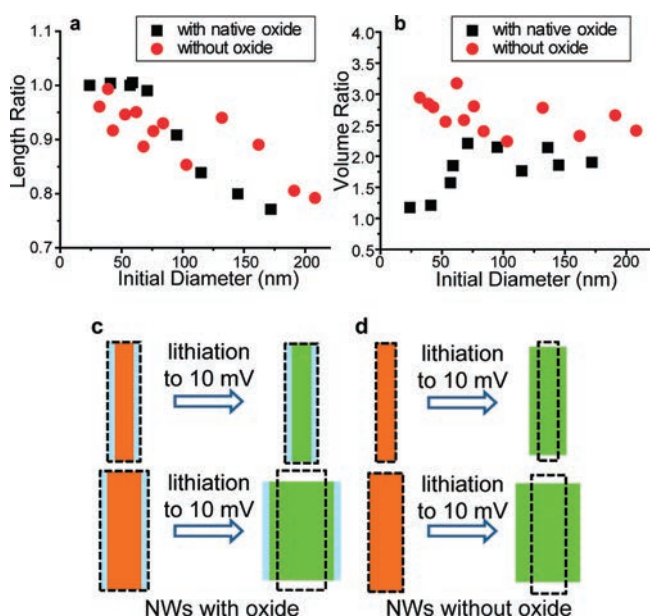
Figure 3. Length and volume changes of Si NWs after lithiating at 10 mV vs Li/Li$^+$. (a) Plot showing length changes (ratio of final length to initial length) after lithiating at 10 mV vs Li/Li$^+$ as a function of initial NW diameter. (b) Plot showing volume changes (ratio of final-to-initial volume) as a function of initial NW diameter after lithiating at 10 mV vs Li/Li$^+$. (c) Schematic summarizing expansion during lithiation of NWs with oxide. Smaller NWs (top) exhibit small diameter and length changes, while larger NWs (bottom) expand in diameter but contract in length. (d) Schematic illustrating expansion during lithiation of NWs without oxide. Smaller and larger NWs (top and bottom, respectively) exhibit diameter expansion and length contraction.

case, the chemical and mechanical properties of the surface layer will be different than the Si core of the NW.

On the basis of this knowledge, we believe a likely contributing factor to the reduced radial expansion in NWs with surface oxide could be a constraining effect; the compounds at the surface could form a relatively strong shell that would mechanically limit the diameter expansion and the extent of lithiation by inducing compressive stress in the NW core during lithiation. Nanoindentation experiments on lithium disilicate (Li$_2$Si$_2$O$_5$) have shown that the hardness, and thus the strength, is rather high (hardness ~6 GPa).[44] In addition, since the shell has nanoscale dimensions, the mechanical strength should be governed primarily by the strength of the atomic bonds in the shell instead of by defect nucleation and mobility, as on the bulk scale. The Li—O and Si—O bonds in the lithiated oxide shell are stronger than the Li—Si bonds in the NW core due to greater ionicity, so it follows that the lithiated shell should be stronger than the core.

To explore this constraining effect, we developed finite element methods for modeling the stresses in NWs of different sizes with and without surface oxide during simulated Li diffusion and concurrent mechanical deformation.[45] In the simulations, the Si core undergoes expansion as it is lithiated, but to simplify the modeling, the oxide shell, which is given the mechanical properties of lithium disilicate,[44] only deforms under mechanical strain and does not expand due to lithiation. The core is given mechanical properties that are a linear interpolation between crystalline Si and amorphous Li—Si.[46,47] The Supporting Information and ref 45 contain more details pertaining to the simulations. Figure 4a shows the effect of a 3.5 nm oxide layer
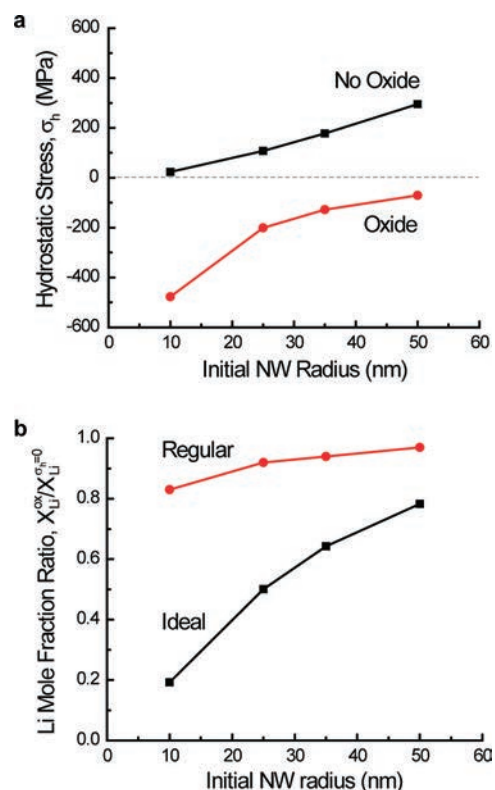

Figure 4. Modeling of stresses and stress effect on mole fraction of Li in the Li—Si phase. (a) Finite element results showing hydrostatic stress at the center of NWs with different initial radius with and without 3.5 nm thick oxide. These stress values are those of greatest magnitude during charging at a rate of 420 mA g^{-1}. NWs without oxide have tensile radial stress, but addition of the oxide layer shifts the stress state toward compression. For the NW with r_i = 10 nm, the oxide causes significant hydrostatic compressive stress (−480 MPa), while the compressive stress diminishes for larger NWs. (b) Thermodynamic estimates of the effect of stress on the equilibrium mole fraction of Li in the Li—Si phase. This plot shows the mole fraction ratio of Li in Si for the oxide case vs the stress-free case ($x_{Li}^{ox}/x_{Li}^{\sigma_i=0}$). For the oxide case, the maximum hydrostatic stress values from the finite element simulations of NWs with oxide were used (panel a). Included in this plot are calculated values using both the ideal solution model ("Ideal") and the regular solution model ("Regular"); see text and Supporting Information for more details.

on the maximum hydrostatic stress present at the center of NWs with different initial radii during lithiation; these maximum stress values result from charging at a rate of 420 mA g^{-1}. Supporting Information Figure S6 contains additional data showing the hydrostatic stress over the cross section for different NW sizes and charging times. As shown in Figure 4a, oxide-free NWs develop diffusion-induced hydrostatic tensile stress during lithiation, but the addition of the oxide layer causes a more compressive stress state to exist in NWs of all sizes. The surface oxide causes significant hydrostatic compression in the smallest NW (initial radius r_i = 10 nm), but the compression effect diminishes as the NW diameter increases. We postulate that this compressive stress could serve to limit the extent of lithiation in the smaller NWs by mechanically constraining the Li—Si expansion and preventing full alloying.

The effect of the compressive stress on the extent of lithiation can be illustrated through the use of thermodynamic estimates. In general, we note that the chemical potential of any component

A (such as Li) in a given phase or mixture is given by

$$\mu_A = \mu_A^0 + RT \ln(a_A) - \Omega\sigma_h \qquad (1)$$

where μ_A^0 is the chemical potential of component A in its reference state, a_A is the activity of component A in the given phase, Ω is the partial molar volume of component A, and σ_h is the hydrostatic stress present. The activity term a_A in eq 1 can be separated into two parts, yielding

$$\mu_A = \mu_A^0 + RT \ln(x_A) + RT \ln(\gamma_A) - \Omega\sigma_h \qquad (2)$$

where x_A is the mole fraction of component A and γ_A is the activity coefficient. The mole fraction term represents the ideal contribution to the chemical potential, where only entropy provides the driving force for mixing, while the activity coefficient term comprises the enthalpic contribution to the chemical potential. For the ideal case, eq 2 becomes

$$\mu_A = \mu_A^0 + RT \ln(x_A) - \Omega\sigma_h \qquad (3)$$

To illustrate the thermodynamic effects of compressive stress on the concentration of Li in the Li–Si phase, we consider both the ideal mixing case and the case in which enthalpic effects are included. These models are obviously simplifications of the actual Li–Si alloying process; for instance, they apply to single-phase solid solutions, whereas the electrochemical reaction of crystalline Si NWs with Li involves a two-phase plateau at about 0.125 V.[33] At lower potentials, however, individual NWs are fully amorphous, which leads to a more sloped galvanostatic voltage plateau,[33] signifying solid-solution-like behavior for which these models could be applied more readily. Even if quantitative accuracy needs to be improved, these simple models are useful because they shed light on possible underlying thermodynamic mechanisms for the experimentally observed behavior.

Because the voltage is held at a fixed value in the ex situ experiments, the chemical potential of Li in the Li–Si alloy should be the same in NWs with an oxide constraining layer (μ_{Li}^{ox}) and NWs that are stress-free ($\mu_{Li}^{\sigma_h=0}$) during lithiation

$$\mu_{Li}^{ox} = \mu_{Li}^{\sigma_h=0} \qquad (4)$$

In this expression, μ_{Li}^{ox} includes the mechanical stress term in eq 2 or 3, while $\mu_{Li}^{\sigma_h=0}$ does not. For the ideal case, combining eqs 3 and 4 and solving for the Li mole fraction ratio in the Li–Si alloy for the oxide versus stress free cases yields

$$\frac{x_{Li}^{ox}}{x_{Li}^{\sigma_h=0}} = \exp\left[\frac{\Omega\sigma_h^{ox}}{RT}\right] \qquad (5)$$

where σ_h^{ox} is the hydrostatic compressive stress in the NWs with oxide. To include enthalpic effects, we employ the regular solution model; in this model, the $RT \ln(\gamma_{Li})$ term in eq 2 is replaced with $\alpha(1 - x_{Li})^2$, where α is a constant that determines the sign and magnitude of the enthalpic interaction. Combining eqs 2 and 4 to compare the oxide vs stress-free cases within the framework of the regular solution model yields the expression

$$\Omega\sigma_h^{ox} = RT \ln\left(\frac{x_{Li}^{ox}}{x_{Li}^{\sigma_h=0}}\right)$$
$$+ \alpha[(1 - x_{Li}^{ox})^2 - (1 - x_{Li}^{\sigma_h=0})^2] \qquad (6)$$

which can be solved for the mole fraction ratio as a function of $x_{Li}^{\sigma_h=0}$.

The magnitudes of the maximum hydrostatic stress from the finite-element simulations (Figure 4a) can be used in conjunction with eqs 5 and 6 to show that the oxide-induced stress could cause a decrease in the equilibrium concentration of Li in the Li–Si phase. Figure 4b shows the Li mole fraction ratio for the oxide case versus the stress-free case for both the ideal model (eq 5) and the regular solution model (eq 6). For the regular solution model, α was fit to be −48 kJ/mol based on the experimental Gibbs free energy of the Li–Si reaction at room temperature (the Supporting Information contains more details about the fitting process). From Figure 4b, both the ideal and regular solution models show that there is a thermodynamic tendency for a decreased concentration of Li in smaller NWs in which the compressive stress is of larger magnitude. The regular solution model yields higher concentrations of Li than the ideal model for all NW sizes because the negative enthalpy of reaction serves to overcome some of the shift in chemical potential due to the compressive stress. Since enthalpic effects are ignored in the ideal model, the regular solution model is probably closer to reality; however, the mole fraction ratio values from the regular solution model could be an underestimate of the actual concentration shift because the entropy of reaction is most likely underestimated with this model. Overall, the finite element simulations combined with these calculations indicate that that the stresses generated in the smallest NWs could be large enough to cause a decrease in the equilibrium Li concentration. This understanding, merged with the fact that the oxide shell expands to a lesser degree than the Si NW itself during lithiation, is a plausible explanation for the experimental observations of decreased volume expansion in the smallest NWs with surface oxide. This conclusion demonstrates that nanoscale control of size, shape, and structure is vital for managing electrochemical characteristics such as capacity.

To determine the effect of NW diameter and oxide thickness on the electrochemical cycling behavior of battery anodes, a half cell configuration was used for galvanostatic tests with Si NWs grown directly on a stainless steel substrate as the working electrode and Li metal as the counter/reference electrode. Figure 5a shows the first charge (lithiation) and discharge (delithiation) of NWs grown from an evaporated 20 nm Au seed layer on stainless steel; these NWs have random diameters ranging from ∼20 to ∼200 nm. The charge and discharge specific capacity with cycling is shown in Figure 5b. The data from three different samples are shown: NWs without an oxide layer, NWs with a ∼3.4 nm thick thermally grown oxide, and NWs with a ∼7.5 nm thick thermally grown oxide. On the first charge, the electrode with oxide-free NWs (black curve) exhibits a sloping potential between ∼1.7 and 0.4 V, whereas the potential curves of both sets of NWs with oxide fall more steeply to ∼0.5 V. Although much of this range is above the usual potential for SEI formation (∼0.4–1.0 V),[48] the sloping potential of the oxide-free NWs indicates the presence of significant side reactions and results in irreversible capacity loss. A previous study on SEI formation on Si NW electrodes has shown that the electrolyte is more readily reduced to form SEI species on NWs without oxide than those with oxide; this can explain the different initial charging slopes in Figure 5a.[48] It is also notable that the initial charge curves for both sets of thermally oxidized NWs show a shoulder at ∼0.5 V. This is not usually observed for as-grown NWs with native oxide.[8] Since the capacity covered by the shoulder is greater for the thicker oxide coating, this suggests that this shoulder is a result of the partial conversion of the surface oxide to Li_2O and Li silicates. Similar conversion potential shoulders are observed in other metal oxide lithiation reactions.[49]
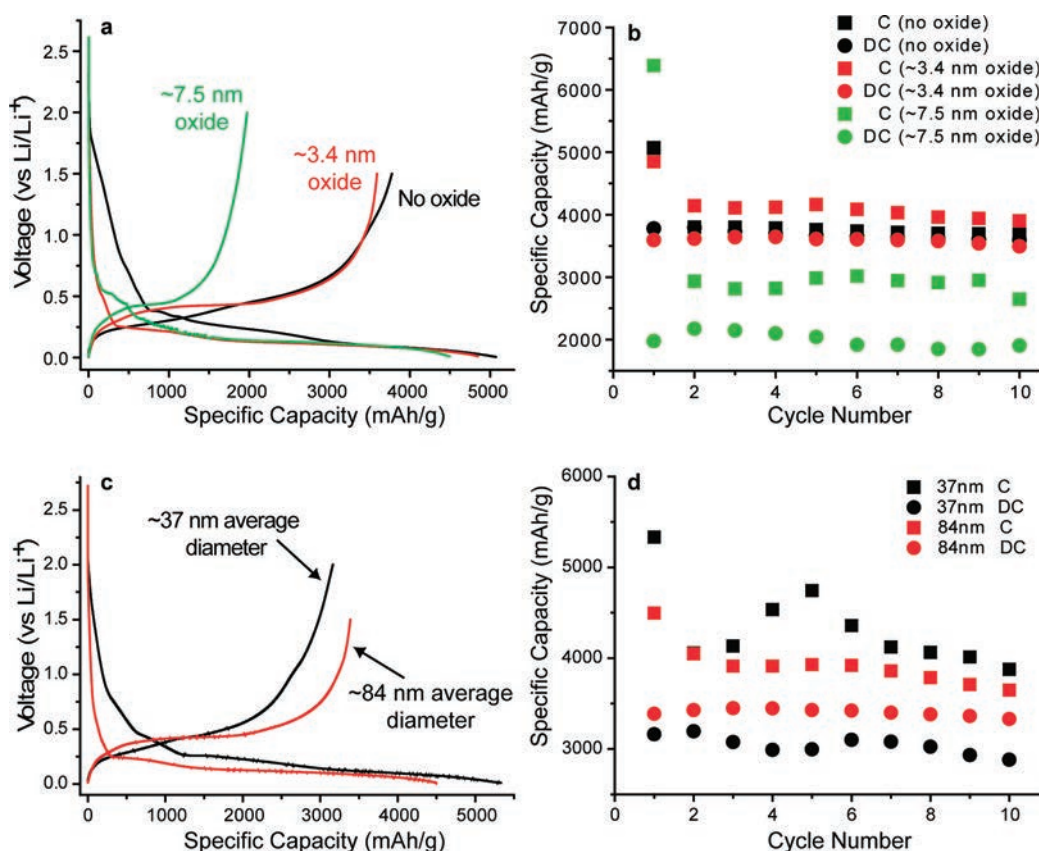
Figure 5. Galvanostatic testing of electrodes with Si NWs of various oxide thicknesses and diameters. (a) First cycle potential profiles for Si NW samples with different oxide thicknesses. (b) Specific capacity with cycling for the samples shown in (a) (C, charge capacity; DC, discharge capacity). (c) First cycle potential profiles for electrodes with Si NWs of different average diameter (37 and 83 nm). The NWs on both electrodes had the same oxide thickness (∼4.5 nm). (d) Specific capacity with cycling for both samples shown in (c). All specific capacity values are calculated by using the mass of Si before oxidation.

Upon first discharge, there is an irreversible capacity loss for all the electrodes, but it is significantly worse for the NWs with thickest oxide (first cycle Coulombic efficiency is ∼30%). The oxide-free NWs show the best Coulombic efficiency with cycling, while the NWs with oxide show lower Coulombic efficiency, as shown in Supporting Information Figure S5. Overall, although the oxide-free NWs show evidence of more significant side reactions on the first charge, they show higher Coulombic efficiency, greater capacity, and more stable cycling behavior than the NWs with oxide. These data shows the importance of the NW surface; the design of a good Si anode must take into account volume expansion concerns and surface chemistry.

Electrochemical tests were also performed on thermally oxidized NWs of different average size. The NWs on the different electrodes were grown from 10 and 100 nm Au nanoparticles, and the average size of the NWs on each electrode was 37 and 83 nm, respectively. Histograms of the measured NW diameters used to compute these average values are presented in Supporting Information Figure S4. After growth, the NWs were thermally oxidized at 600 °C for 5 min, which causes an ∼4.4 nm oxide layer to form on all NWs. The first charge and discharge curves for both sets of NWs are shown in Figure 5c, and the specific capacity with cycling is shown in Figure 5d. The charge and discharge curves for the smaller (black) and larger (red) NWs are similar, except that there is more irreversible capacity loss in the first cycle in the smaller NWs due to more SEI

formation. This is because of the greater surface area available for side reactions in the smaller NWs. From Figure 5d, the larger NWs show higher discharge capacity and better Coulombic efficiency over 10 cycles. However, the Coulombic efficiency is still below 95% for the thicker NWs, which shows that the oxide contributes to irreversible capacity loss even for the larger NWs.

These electrochemical data relate to the dimensional expansion measurements of individual NWs in a number of ways. First, the NWs with the thickest thermally grown oxide exhibit the least diameter expansion upon lithiation for all diameters (Figure 2d), and they provide the lowest charge and discharge capacity with cycling (Figure 5b). This is consistent with our previous explanation regarding the oxide shell; the lower capacity could partly be due to the constraining effect of the thicker oxide, which serves to limit volume expansion and extent of lithiation. The lower volume fraction of Si in the NWs with thicker oxide could also contribute to the lower capacity. In addition, the oxide-free NWs exhibit the highest specific capacity and Coulombic efficiency after the first cycle. The lack of an oxide layer could allow for relatively unhindered volume expansion for NWs of all sizes along with diminished side reactions after the first cycle, which results in good cycling.

In summary, we have studied the effect of Si NW size and surface oxide thickness on the dimensional changes and cycling behavior during reaction with Li. A surface oxide was shown to affect the diameter and volume expansion of Si NWs of different

sizes upon lithiation; smaller NWs with surface oxide expand to a lesser degree than larger NWs. Finite element modeling was used to show that even a thin oxide layer can induce hydrostatic compressive stress that increases in magnitude with decreasing NW size, and this stress has a thermodynamic tendency to cause a decrease in the equilibrium concentration of Li in the Li—Si phase. Finally, the electrochemical cycling behavior of NWs with and without oxide and of different average diameter was also investigated. NWs without oxide undergo more side reactions during the first lithiation but exhibit higher capacity and more stable cycling behavior than NWs with oxide layers. Overall, our results indicate that the oxide thickness and NW size critically affect dimensional expansion and electrochemical cycling characteristics. This is important since the volume changes and stresses in Si electrodes play a large role in determining the cycle life. These findings can be directly applied to improving nanostructured Si electrodes through the precise control of volume expansion. For instance, since compressive stress has a thermodynamic tendency to limit the extent of lithiation, this must be taken into account when designing nanostructures for Si electrodes. In addition, an external constraining layer could be used in hollow nanostructures to cause desirable volume expansion away from the outer surface, which would minimize the increase in outer surface area during reaction and allow for stable SEI formation.

Methods. *Si NW Growth.* Si NWs were grown by the vapor—liquid—solid (VLS) process. For the size-dependence and oxide studies (data in Figures 2, 3, and 5a,b), a 20 nm Au film was evaporated onto 304 stainless steel substrates (McMaster-Carr) that were then situated inside a quartz tube (1 in. diameter) in a tube furnace. The substrates were heated pregrowth to 485 °C for 20 min under vacuum. In the subsequent growth step, 2% silane (SiH_4) gas in argon was flowed through the tube at 50 sccm and at a constant pressure of 40 Torr for 30 min. The temperature was kept at 485 °C during the growth step. This NW growth process produces NWs of varying diameter.

For the growth of Si NWs with more uniform diameter as used to obtain the data in Figure 5c,d, Au nanoparticles were used as the catalyst for VLS growth.[50] Stainless steel substrates were first treated with O_2 plasma for 3 min and then a poly-L-lysine solution (0.1% w/v aqueous, Ted Pella) was coated on the substrates to enhance the adhesion of gold nanoparticles. The poly-L-lysine was rinsed off after two minutes. Next, Au nanoparticles with average diameter of 10 and 100 nm (Ted Pella) were placed on the substrates and gently washed away after two minutes. The substrates with Au nanoparticles were again treated with O_2 plasma for three minutes. For the growth process, the same setup was used as before but with modified growth conditions: 480 °C, 50 sccm, 25 min growth time, and 30 and 25 Torr pressure for the 100 and 10 nm Au nanoparticles, respectively.

Oxide Thickness Control. To control the thickness of the oxide layer on the NWs, different annealing temperatures were employed. As-grown Si NWs were first dipped in 13% HF for 30 s to remove the native oxide. The Si NWs were then annealed in a box furnace in air. The temperature was increased to the desired value during a 30 min linear ramp and then was maintained at that temperature for 5 min. After this process was complete, the furnace was turned off and allowed to naturally cool to room temperature. Annealing at 500, 600, and 750 °C generates ~3.4, 4.5, and 7.5 nm thick oxide layers, respectively (Supporting Information Figure S2).

Electrochemistry and Characterization. For the ex situ TEM technique, TEM grids with reference marks (Ted Pella) were used. A 20 nm Ti film was first deposited by e-beam evaporation onto the 15—25 nm thick amorphous carbon films on the grids to ensure good electrical contact between the NWs and the TEM grids. The NWs were then removed from their growth substrates by sonication and suspended in methanol. Several drops of the NW suspension were placed onto the TEM grids, and the methanol was allowed to evaporate. After this step, the grids were placed in the TEM (200 kV FEI Tecnai F20), and single NWs were located and imaged. The TEM grids were then inserted directly into pouch-type half cells in which they behaved as current collectors to facilitate the charge and discharge of the Si NWs at the surface. Li metal foil was used as the counter and reference electrode, and both electrodes were contacted with Cu foil current collectors. Separators (Asahi Kasei) soaked with electrolyte (1 M $LiPF_6$ in ethylene carbonate/diethyl carbonate (EC/DEC), 1:1 v/v, Ferro Corporation) were placed between the two electrodes. The half cell layout is shown schematically in Figure 1c.

For charge and discharge of the half cells, a linear sweep voltammetry technique was used on a Biologic VMP3 battery tester. All potentials are quoted with regard to the Li/Li^+ redox potential. For lithiation (charge), the voltage of the NW electrode was swept from the open circuit potential (~2.5 V) to 10 mV at a scan rate of 0.2 mV/s. The NW electrode was held at 10 mV versus Li/Li^+ for 48 h. After the electrochemical treatment, the TEM grids were removed from the half cells in an Ar-filled glovebox, rinsed thoroughly with acetonitrile to remove excess SEI, and then transported to the TEM in sealed glass vials. The samples were loaded into the TEM chamber in less than 15 s after opening the sample vial to minimize their exposure to air. The same NWs that were originally imaged were located and imaged again.

For the data in Figure 5, galvanostatic charging and discharging was used instead of the potentiostatic method described previously. All galvanostatic measurements were performed at a rate of C/10, which corresponds to complete charge or discharge in 10 h. For these experiments, the NW electrodes consisted of Si NWs grown directly on stainless steel current collectors.

■ ASSOCIATED CONTENT

ⓢ Supporting Information. Additional information and figures. This material is available free of charge via the Internet at http://pubs.acs.org.

■ AUTHOR INFORMATION

Corresponding Author
*E-mail: (J.W.C.) jangwookchoi@kaist.ac.kr; (Y.C.) yicui@stanford.edu.

Author Contributions
§These authors contributed equally to this work.

■ ACKNOWLEDGMENT

■ REFERENCES

(1) Armand, M.; Tarascon, J. M. *Nature* **2008**, *451* (7179), 652–657.

(2) Whittingham, M. S. *MRS Bull.* **2008**, *33* (4), 411–419.

(3) Ji, X. L.; Lee, K. T.; Nazar, L. F. *Nat. Mater.* **2009**, *8* (6), 500–506.

(4) Sun, Y. K.; Myung, S. T.; Park, B. C.; Prakash, J.; Belharouak, I.; Amine, K. *Nat. Mater.* **2009**, *8* (4), 320–324.

(5) Ogasawara, T.; Debart, A.; Holzapfel, M.; Novak, P.; Bruce, P. G. *J. Am. Chem. Soc.* **2006**, *128* (4), 1390–1393.

(6) Kasavajjula, U.; Wang, C. S.; Appleby, A. J. *J. Power Sources* **2007**, *163* (2), 1003–1039.

(7) Magasinski, A.; Dixon, P.; Hertzberg, B.; Kvit, A.; Ayala, J.; Yushin, G. *Nat. Mater.* **2010**, *9* (4), 353–358.

(8) Chan, C. K.; Peng, H. L.; Liu, G.; McIlwrath, K.; Zhang, X. F.; Huggins, R. A.; Cui, Y. *Nat. Nanotechnol.* **2008**, *3* (1), 31–35.

(9) Arico, A. S.; Bruce, P.; Scrosati, B.; Tarascon, J. M.; Van Schalkwijk, W. *Nat. Mater.* **2005**, *4* (5), 366–377.

(10) Huggins, R. A. *J. Power Sources* **1999**, *81*, 13–19.

(11) Cui, L. F.; Ruffo, R.; Chan, C. K.; Peng, H. L.; Cui, Y. *Nano Lett.* **2009**, *9* (1), 491–495.

(12) Kim, H.; Seo, M.; Park, M. H.; Cho, J. *Angew. Chem., Int. Ed.* **2010**, *49* (12), 2146–2149.

(13) Song, T.; Xia, J. L.; Lee, J. H.; Lee, D. H.; Kwon, M. S.; Choi, J. M.; Wu, J.; Doo, S. K.; Chang, H.; Il Park, W.; Zang, D. S.; Kim, H.; Huang, Y. G.; Hwang, K. C.; Rogers, J. A.; Paik, U. *Nano Lett.* **2010**, *10* (5), 1710–1716.

(14) Yu, Y.; Gu, L.; Zhu, C. B.; Tsukimoto, S.; van Aken, P. A.; Maier, J. *Adv. Mater.* **2010**, *22* (20), 2247–2250.

(15) Zhou, S.; Liu, X. H.; Wang, D. W. *Nano Lett.* **2010**, *10* (3), 860–863.

(16) Park, M. H.; Kim, M. G.; Joo, J.; Kim, K.; Kim, J.; Ahn, S.; Cui, Y.; Cho, J. *Nano Lett.* **2009**, *9* (11), 3844–3847.

(17) Beaulieu, L. Y.; Eberman, K. W.; Turner, R. L.; Krause, L. J.; Dahn, J. R. *Electrochem. Solid-State Lett.* **2001**, *4* (9), A137–A140.

(18) Chevrier, V. L.; Dahn, J. R. *J. Electrochem. Soc.* **2009**, *156* (6), A454–A458.

(19) Huggins, R. A.; Nix, W. D. *Ionics* **2000**, *6*, 57–63.

(20) Cheng, Y. T.; Verbrugge, M. W. *J. Power Sources* **2009**, *190* (2), 453–460.

(21) Deshpande, R.; Cheng, Y. T.; Verbrugge, M. W. *J. Power Sources* **2010**, *195* (15), 5081–5088.

(22) Golmon, S.; Maute, K.; Lee, S. H.; Dunn, M. L. *Appl. Phys. Lett.* **2010**, *97* (3), 033111.

(23) Hertzberg, B.; Alexeev, A.; Yushin, G. *J. Am. Chem. Soc.* **2010**, *132* (25), 8548.

(24) Beaulieu, L. Y.; Hatchard, T. D.; Bonakdarpour, A.; Fleischauer, M. D.; Dahn, J. R. *J. Electrochem. Soc.* **2003**, *150* (11), A1457–A1464.

(25) Lee, S. W.; McDowell, M. T.; Choi, J. W.; Cui, Y. *Nano Lett.* **2011**, *11* (7), 3034–3039.

(26) Goldman, J. L.; Long, B. R.; Gewirth, A. A.; Nuzzo, R. G. *Adv. Funct. Mater.* **2011**, *21* (13), 2412–2422.

(27) Liu, X. H.; Zheng, H.; Zhong, L.; Huang, S.; Karki, K.; Zhang, L. Q.; Liu, Y.; Kushima, A.; Liang, W. T.; Wang, J. W.; Cho, J.-H.; Epstein, E.; Dayeh, S. A.; Picraux, S. T.; Zhu, T.; Li, J.; Sullivan, J. P.; Cumings, J.; Wang, C.; Mao, S. X.; Ye, Z. Z.; Zhang, S.; Huang, J. Y. *Nano Lett.* **2011**, *11* (8), 3312–3318.

(28) Liu, X. H.; Zhang, L. Q.; Zhong, L.; Liu, Y.; Zheng, H.; Wang, J. W.; Cho, J.-H.; Dayeh, S. A.; Picraux, S. T.; Sullivan, J. P.; Mao, S. X.; Ye, Z. Z.; Huang, J. Y. *Nano Lett.* **2011**, *11* (6), 2251–2258.

(29) Ma, D. D. D.; Lee, C. S.; Au, F. C. K.; Tong, S. Y.; Lee, S. T. *Science* **2003**, *299* (5614), 1874–1877.

(30) Hu, Y. S.; Demir-Cakan, R.; Titirici, M. M.; Muller, J. O.; Schlogl, R.; Antonietti, M.; Maier, J. *Angew. Chem., Int. Ed.* **2008**, *47* (9), 1645–1649.

(31) Su, L. W.; Zhou, Z.; Ren, M. M. *Chem. Commun.* **2010**, *46* (15), 2590–2592.

(32) Morales, A. M.; Lieber, C. M. *Science* **1998**, *279* (5348), 208–211.

(33) Chan, C. K.; Ruffo, R.; Hong, S. S.; Huggins, R. A.; Cui, Y. *J. Power Sources* **2009**, *189* (1), 34–39.

(34) Kang, K.; Lee, H. S.; Han, D. W.; Kim, G. S.; Lee, D.; Lee, G.; Kang, Y. M.; Jo, M. H. *Appl. Phys. Lett.* **2010**, *96* (5), 3.

(35) Limthongkul, P.; Jang, Y. I.; Dudney, N. J.; Chiang, Y. M. *Acta Mater.* **2003**, *51* (4), 1103–1113.

(36) Key, B.; Bhattacharyya, R.; Morcrette, M.; Seznec, V.; Tarascon, J. M.; Grey, C. P. *J. Am. Chem. Soc.* **2009**, *131* (26), 9239–9249.

(37) Li, H.; Huang, X. J.; Chen, L. Q.; Zhou, G. W.; Zhang, Z.; Yu, D. P.; Mo, Y. J.; Pei, N. *Solid State Ionics* **2000**, *135* (1–4), 181–191.

(38) Obrovac, M. N.; Christensen, L. *Electrochem. Solid-State Lett.* **2004**, *7* (5), A93–A96.

(39) Hatchard, T. D.; Dahn, J. R. *J. Electrochem. Soc.* **2004**, *151* (6), A838–A842.

(40) Nagao, Y.; Sakaguchi, H.; Honda, H.; Fukunaga, T.; Esaka, T. *J. Electrochem. Soc.* **2004**, *151* (10), A1572–A1575.

(41) Miyachi, M.; Yamamoto, H.; Kawai, H.; Ohta, T.; Shirakata, M. *J. Electrochem. Soc.* **2005**, *152* (10), A2089–A2091.

(42) Netz, A.; Huggins, R. A.; Weppner, W. *J. Power Sources* **2003**, *119*, 95–100.

(43) Sun, Q.; Zhang, B.; Fu, Z. W. *Appl. Surf. Sci.* **2008**, *254* (13), 3774–3779.

(44) Soares, P. C.; Lepienski, C. M. *J. Non-Cryst. Solids* **2004**, *348*, 139–143.

(45) Ryu, I.; Choi, J. W.; Cui, Y.; Nix, W. D. *J. Mech. Phys. Solids* **2011**, DOI: 10.1016/j.jmps.2011.06.003.

(46) Sethuraman, V. A.; Chon, M. J.; Shimshak, M.; Srinivasan, V.; Guduru, P. R. *J. Power Sources* **2010**, *195* (15), 5062–5066.

(47) Bhandakkar, T. K.; Gao, H. J. *Int. J. Solids Struct.* **2010**, *47* (10), 1424–1434.

(48) Chan, C. K.; Ruffo, R.; Hong, S. S.; Cui, Y. *J. Power Sources* **2009**, *189* (2), 1132–1140.

(49) Idota, Y.; Kubota, T.; Matsufuji, A.; Maekawa, Y.; Miyasaka, T. *Science* **1997**, *276* (5317), 1395–1397.

(50) Patolsky, F.; Zheng, G. F.; Lieber, C. M. *Nat. Protoc.* **2006**, *1* (4), 1711–1724.